Chaotic Modeling and Simulation (CMSIM) 1: 19–30, 2013

Pattern Formation in Volumetrically Heated Fluids

Gregory Cartland Glover[1] Kaoru Fujimura[2] and Sotos Generalis[3]

[1] Marie Curie IE Fellow, Mathematics, Aston University, Birmingham B4 7ET, UK
(E-mail: g.cartland-glover@aston.ac.uk)
[2] Applied Mathematics and Physics, Tottori University, Tottori 680-8552, Japan
(E-mail: kaoru@damp.tottori-u.ac.jp)
[3] Mathematics, Aston University, Birmingham B4 7ET, UK
(E-mail: s.c.generalis@aston.ac.uk)

Abstract. Finite element simulations have been performed along side normal mode analysis on the linear stability that examined the development of volumetrically heated flow patterns in a horizontal layer controlled by the Prandtl number, Pr, and the Grashof number, Gr. The fluid was bounded by an isothermal plane above an adiabatic plane. In the simulations performed here, a number of convective polygonal planforms occurred, as Gr increased above the critical Grashof number, Gr_c at $Pr = 7$, while roll structures were observed for $Pr < 1$ at $2Gr_c$.
Keywords: Non-linear, bifurcation, stability, volumetric heating, asymmetric boundaries.

1 Introduction

This work is concerned with the numerical simulation of the early stage transition regime of an internally heated fluid layer situated between a conducting upper boundary and an insulating lower boundary. The study described here is motivated by earlier studies [4,6,8] and the importance such flow structures have in the development of flows that are found in many engineering and geophysical applications.

Examples of volumetric heating cover thermal convection driven by the radioactive decay of fluid components. Asfia and Dhir [2] who studied thermal convection in a pool that mimicked the motion caused by fission product decay in the molten fuel elements that collect in the lower head of a nuclear reactor during a severe accident. Briant and Weinberg [3] devised the molten salt nuclear reactor concept, where the fissile material is dissolved in the coolant and thus provides volumetric heating to the fluid phase. Geophysical flows in the Earth's mantle are driven by radioactive decay [5,10,15,16]. Tritton and Zarraga [20], Tasaka *et al.* [18], Takahashi *et al.* [17] have studied the

Received: 29 November 2012 / Accepted: 22 January 2013

ISSN 2241-0503

phenomena experimentally using various approaches to generate fluid motion and record the structures observed.

Several numerical studies of thermal convection driven by internal heating have been performed using a variety of techniques to resolve the evolving circulation cells via the application of mean field approximations ([14]), expansions in orthogonal functions of finite amplitudes used in pseudospectral techniques ([8], [10], [15], [16], [9], [22], [19]) and finite volume or element approaches ([6], [11]).

Cartland Glover and Generalis [6] (hereafter indicated as CCG) focussed on domains with aspect ratios of $\left\{1 : 4\sqrt{3} : 12\right\}$ suggested by Ichikawa *et al.* [11]. Several types of circulation cells were observed by CGG [6], as the Grashof number, Gr, was increased, which corresponded to observatiosn of Roberts [14] at transition and to Tveiteried and Palm [22] at higher Gr. There were two key factors that affected the development of the circulation cells in CGG [6]. These were how the internal heating conditions were defined and the influence of the periodic conditions on the flow field. CGG [6] assumed an equivalent constant temperature difference of the applied heating and varied the depth between the parallel plates to control Gr and the internal heating supplied, which is not consistent with experimentation [20,18,17].

Thus, the motivation for this new study is two-fold: we are interested in reducing the error from the simulations in the wavenumber, which were observed around the critical transition and we would like to compare the numerical results obtained with the experimental results [20,18,17]. Note that in the finite element simulations performed here, the variation of the internal heating condition was driven by the varying temperature difference rather than modifying the depth between the parallel planes, the former of which is more consistent with experimental methods of Tasaka *et al.* [18] and Takahashi *et al.* [17] for example. To try to reduce the influence of the periodic boundary conditions and the any effect that the domain aspect ratio has on the formation of structures, the extent of the domain was also increased from $\left\{1 : 4\sqrt{3} : 12\right\}$ to $\{1 : 12 : 12\}$.

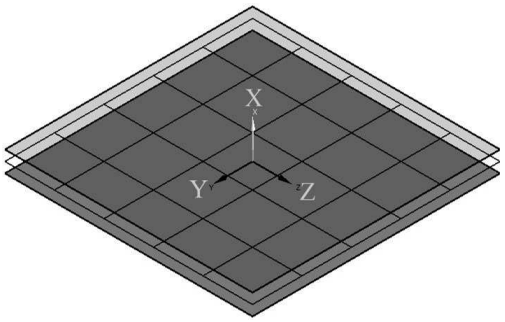

Fig. 1. Diagram of the homogeneous layer with an isothermal surface above an adiabatic surface. The coordinate axis is at the origin and the midplane surface is also indicated by the coarse grid.

2 Theory

We consider a volumetrically heated viscous incompressible fluid in a horizontal layer of width L bounded by plates of infinite extent (Figure 1). The upper plate is a conducting surface and the lower plate is an insulating surface. The cartesian coordinate system is located on the midplane of the layer (Figure 1). We start by following the Navier-Stokes equations for the velocity vector $\boldsymbol{u}$ and the pressure, p, and a transport equation for the temperature, T, from the environment

$$\nabla \cdot \boldsymbol{u} = 0,$$

$$\rho \frac{\partial \boldsymbol{u}}{\partial t} + \rho \left(\boldsymbol{u} \cdot \nabla \right) \boldsymbol{u} = -\nabla p + \mu \nabla^2 \boldsymbol{u} - \boldsymbol{g} \rho \beta \left(T - T_r \right),$$

$$\rho \frac{\partial T}{\partial t} + \rho \left(\boldsymbol{u} \cdot \nabla \right) T = \rho k \nabla^2 T + S_i,$$

where $\boldsymbol{g}$ is the acceleration due to gravity, k is the thermal conductivity, S_i is the volumetric heat source, T_r is the reference temperature of the fluid modelled and β is the thermal expansion coefficient.

2.1 Conditions Applied

We apply L, L^2/ν and $\Delta T_i = \left(Gr\mu^2 \right) / \left(g\rho^2\beta \ L^3 \right)$, as the units of length, time and temperature to non-dimensionalise the system. This gives $\boldsymbol{\upsilon}$, ϖ and θ as the non-dimensionalised velocity vector, pressure and temperature, respectively.

We obtain two non-dimensional numbers, which control the volumetric heating supplied to the horizontal layer and the influence of the thermal diffusivity. These are the Grashof number with the form $Gr = \left(g\rho^2\beta S_i L^5 \right) / \left(2\mu^2 k \right)$ and the Prandtl number, $Pr = \left(c_p \mu \right) / k$. The fluid properties are defined by the specific heat capacity at constant pressure, c_p, dynamic viscosity, μ and the density, ρ. Several Gr over the range $1 \leq \varepsilon \leq 12$ were selected in order to vary the temperature difference at $Pr = 7$ and therefore the heat flux applied, where $\varepsilon = Gr/Gr_c$. Then Pr was varied to observe the influence of thermal diffusion on the resolved flow states. The product of Grashof number and the Prandtl number gives the Rayleigh number.

The boundary conditions are $\theta|_{x=1} = 0$, $\partial_x \theta|_{x=0} = 0$, $\boldsymbol{\upsilon}|_{x=0} = \boldsymbol{\upsilon}|_{x=1} = 0$ and the initial conditions are $\theta = 0$ and $\boldsymbol{\upsilon} = 0$. We assume the Boussinesq approximation applies to the definition of the fluid phases and the volumetrically applied heating.

The treatment (described below) of the non-dimensional numbers and the initial and boundary conditions differs between the numerical simulations by means of the finite element method and the linear stability analysis.

2.2 Linear stability analysis

To perform the linear stability analysis we start with the non-dimensional form of the governing equations:

$$\nabla \cdot \boldsymbol{\upsilon} = 0,$$

$$\frac{\partial \boldsymbol{\upsilon}}{\partial t} + (\boldsymbol{\upsilon} \cdot \nabla)\, \boldsymbol{\upsilon} = -\nabla \varpi + \nabla^2 \boldsymbol{\upsilon} - \frac{\boldsymbol{g}}{g}\theta,$$

$$\frac{\partial \theta}{\partial t} + (\boldsymbol{\upsilon} \cdot \nabla)\, \theta = \frac{1}{Pr}\left(\nabla^2 \theta + 2Gr\right),$$

The basic field in the conduction state without macroscopic flow is due to a static balance of the pressure with the buoyancy force. Under the imposed boundary conditions the basic temperature, $\bar{\theta}$, is given by $Gr(x^2 + 2x - 3)/2$ [14], where x is non-dimensionalised by L and t by L^2/ν.

Let us denote the deviation of $\boldsymbol{\upsilon}$, ϖ, and θ from the basic field by $\hat{\boldsymbol{\upsilon}}$, $\hat{\varpi}$, and $\hat{\theta}$. We linearize the governing equations for the disturbance, and assume the normal mode such that

$$\begin{pmatrix} \hat{\boldsymbol{\upsilon}} \\ \hat{\varpi} \\ \hat{\theta} \end{pmatrix} \propto \begin{pmatrix} \boldsymbol{\Upsilon}(x) \\ \mathit{\Pi}(x) \\ \Theta(x) \end{pmatrix} e^{\sigma t + \imath(\alpha_y y + \alpha_z z)}$$

We substitute this expression into the linearized governing equations. The resulting ODEs for the 'amplitude functions of the normal mode', $\boldsymbol{\Upsilon}(x)$, $\mathit{\Pi}(x)$, and $\Theta(x)$, form a linear eigenvalue problem under non-slip boundary conditions, $\boldsymbol{\Upsilon} = 0$ at $x = 0$ and 1 and the thermal boundary conditions $\Theta = 0$ at x = 1 and $\Theta' = 0$ at $x = 0$.

At this stage, we introduced the toroidal-poloidal decomposition to eliminate $\mathit{\Pi}(x)$. See [8,12] for details. We discretize the amplitude functions by means of an expansion in Chebyshev polynomials. Applying the collocation method together with tau method, we reduce the linear eigenvalue problem corresponding to two-point boundary value problem to an algebraic linear eigenvalue problem of the form $A\boldsymbol{x} = \sigma B\boldsymbol{x}$, which is solved numerically by means of the QZ algorithm. Twenty polynomials are used to resolve the neutral curves presented here.

At the end of this subsection, we note that since the basic field has Euclidean symmetry E(2) on the yz-plane, there is no preferred direction there. This implies that a wave vector (α_y, α_z) on two-dimensional wave plane does not appear in the eigenvalue problem. Instead, the wavenumber $\alpha = \sqrt{\alpha_y^2 + \alpha_z^2}$ is involved.

2.3 Simulation method

As the solver used in the finite element method used dimensional equations [1], it is necessary to specify $S_i = (2k\Delta T_i)/L^2$ in terms of Gr (see below) and $L = 0.007$ m, which was defined according to the experimental studies of Tasaka *et al.* [18]. Periodic conditions are applied to the vertical surfaces of

the domain Figure 1. Please refer to CGG [6] for a thorough description of the specifications required to perform the finite element method simulations. Key exceptions from CGG [6] are the domain used, which was a square layer with an aspect ratio of $\{1:12:12\}$ that had the respective node resolution of $\{30:180:180\}$ and the assumed physical time-scale, $c_p\rho L^2/k$, to control the rate of convergence.

3 Results

The resultant solutions for convection caused by volumetrically heating a horizontal layer show the deviations from the conductive laminar state. At $Pr = 7$, the transition from conductive to convective flow occurs at Gr_c= 198, which corresponds to $Ra_c = 1386$ ([14], [11], [22]). The structures are indicated by the change in characteristic parameters, which are plotted between Figure 2 and Figure 5. Figure 2 presents the neutral curves obtained by the linear analysis. Contour plots of the temperature and the vertical velocity component for $Pr = 7$, where $\varepsilon = 1$, 2, 3, 6 and 12 are illustrated in Figure 3. The change of velocity components and the temperature with ε are plotted in Figure 4. Contour plots of the temperature and the vertical velocity component for Pr = 0.005, 0.705, 0.883 and 8.933 are given in Figure 5.

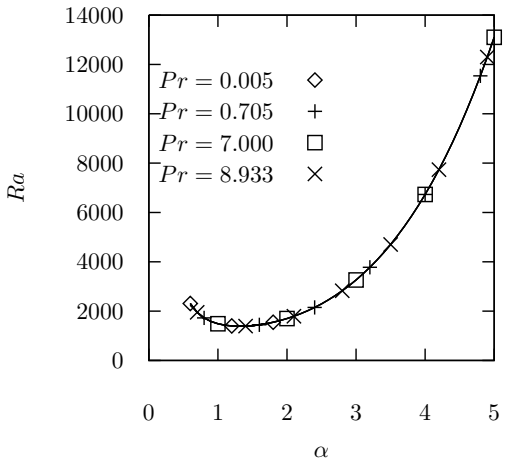

Fig. 2. Neutral curves of stability (solid lines) obtained from the linear normal mode analysis, where α is the wavenumber.

3.1 Fluids with Pr=7

The neutral curves obtained from the linear normal mode analysis are given in Figure 2, where the curves indicate the highest value allowed by the linear analysis for the basic state to retain its laminar form.

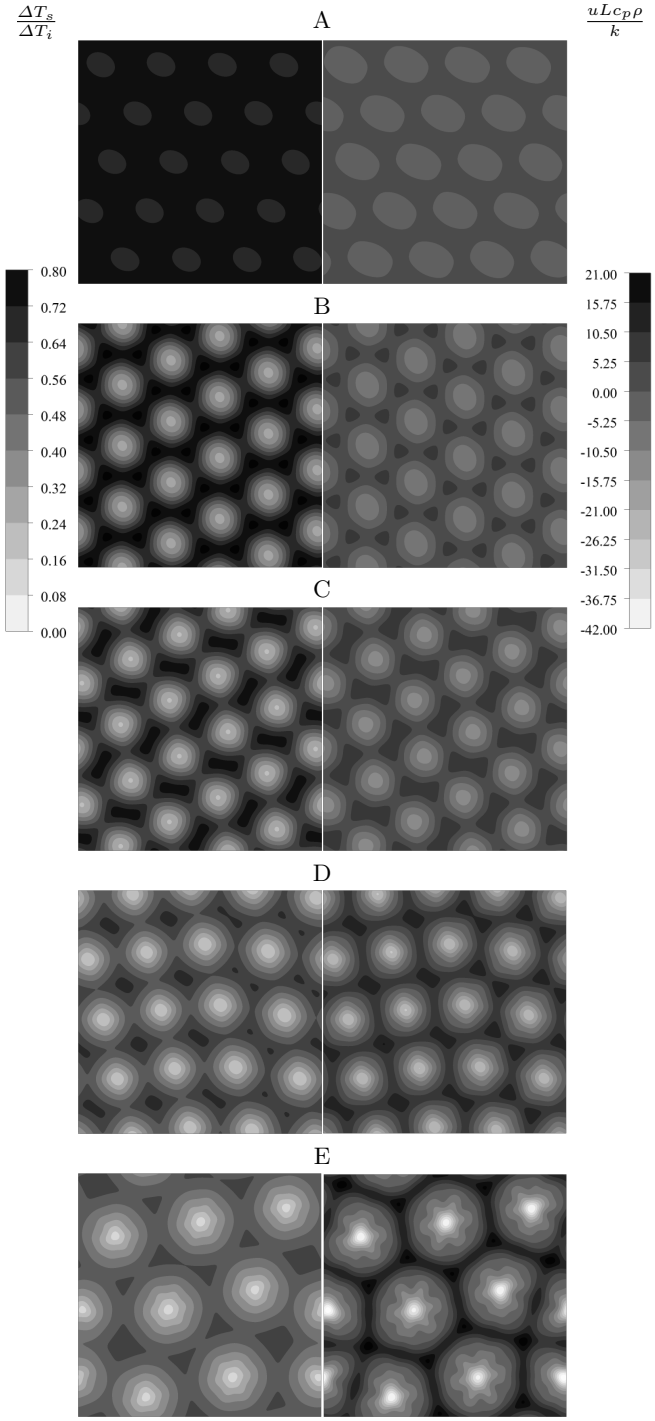

Fig. 3. Non-dimensional temperature (left) and vertical velocity (right) contours on the midplane in Figure 1, for Pr=7 . Here $\Delta T_s/\Delta T_i = |T - T_{\min}|_s / \left(Gr\mu^2\right) / \left(g\rho^2\beta\ L^3\right)$. A: $\varepsilon = 1$; B: $\varepsilon = 2$; C: $\varepsilon = 3$; D: $\varepsilon = 6$; E: $\varepsilon = 12$.

At ε=1, Figure 3 already shows non-vanishing hexagonal pattern. This is due to the fact that the solution branch of the down-hexagons bifurcates subcritically i.e. ε <1, as reported by Tveitereid and Palm [22]. Indeed, the branch of stable down-hexagons ends up with a limit point (or saddle-node point) at which the stable upper branch is connected with the lower branch of the transcritical bifurcation stemmed subcritically from the bifurcation point ε=1. The stable down-hexagons are generated in the following sequence: hexagons true to the y axis at $\varepsilon = 1$ (Figure 3A), hexagons perpendicular to the y axis (Figure 3B), hexagons aligned at $\sim 50^{\circ}$ to y axis (Figure 3C), polygonal structures (Figure 3D), hexagons with spokes (Figure 3E). Note that the change in the alignment of the hexagons between Figure 3A and 3C indicates that there is no preference in the orientation of the hexagons.

The structures depicted in Figure 3 are qualitatively comparable with the experimental studies of Takahashi *et al.* [17] and Tasaka *et al.* [18], where measurements of the temperature field [18] and the velocity field [17] were made for $\varepsilon \in (3, 6)$. These conditions correspond to cases C and D presented in Figure 3. The increase in the size of the circulation cell is of a similar magnitude in both the experiments and the simulation. The range of vertical velocities observed in the simulations described are similar to those reported by Takahashi *et al.* [17].

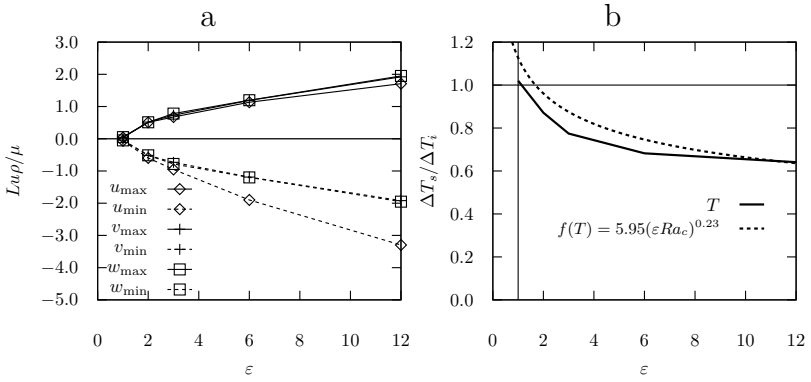

Fig. 4. Profiles against ε obtained from the finite element code. a) The maximum and the minimum values of the velocity components; b) $\Delta T_s/\Delta T_i = T_{\max} - T_{\min}/\left(Gr\mu^2\right)/\left(g\rho^2\beta\ L^3\right)$, where s refers to the temperature extracted from the solved flow field. $f(T) = 5.95(\varepsilon * Ra_c)^{-0.23}$, an empirical profile given by Turcotte *et al.* [21]; horizontal line: conduction condition; vertical line: transition between conduction and convection.

In Figure 4 we show the change of key variables with ε for the simulations using the finite element code. A significant increase in all the velocity components at $\varepsilon = 1$ in Figure 4a. The increases in the velocity are associated with the change in the state of the fluid layer at the critical transition, where we conjecture that isotropic hexagons are formed. The patterns formed are

considered to be isotropic as the minima and maxima of the v and w display similar magnitudes.

The down-welling minimum velocity indicated in Figure 11 of Takahashi *et al.* [17] gave vertical velocities, which were approximately one third less than the vertical velocities in Figure 4a. This difference could be due to methods used to assess the minimum vertical velocity or the influence of the heat flux across the lower boundary used. The minimum vertical velocity of Takahashi *et al.* [17] was determined from the planes defined by the laser sheets used for their PIV measurements, while the velocities in Figure 4a are the minimum and maximum values for the whole of the simulated domain.

The effect of the transition from conductive to convective flow is also shown by the change in the temperature difference relative to the initial or conductive temperature difference (Figure 4b). At higher heat fluxes the temperature difference caused by convection drops below the conductive temperature difference. This is due to the influence that cellular convection has on the layer as energy from the volumetric heat source is used to drive the fluids across the layer [5]. A portion of the internal heating supplied is also lost from the system through the top isothermal boundary [20]. An empirical relation of the decrease in the temperature difference due to convection is also plotted in Figure 4 [21].

3.2 Other fluids

To confirm the secondary flows predicted by the finite element code soon after Gr_c show behaviour consistent with literature, fluids of different Pr were tested for $\varepsilon = 2$ (Figure 5). For $Pr < 1$, the circulation cells take the form of steady ($0.5 < \mathrm{Pr} < 1$) or unsteady ($Pr < 0.1$) two-dimensional rolls. While a mix of polygonal structures occur for $Pr = 8.933$. For $Pr \simeq 0.70$ dislocations in the roll structures are also observed, which may disappear in time-averaged plots obtained from a time-marching solution. For $Pr \simeq 0.85$, where supercritical or high pressure fluids were considered within CFX, large variations in the fluid density can occur for small changes in the temperature [13]. Therefore, in the limit of the Boussinesq approximation (i.e. constant density), the heating condition we applied resulted in small non-measureable differences in the temperature. This lead to the formation of sharply defined differences in the temperature.

4 Conclusions

The main interest in the present work is the hierarchical transition from conductive flow to convective flow and on to the turbulent regime in an asymmetric horizontal layer. We have concentrated on the stability boundary of the basic state in order to compare states found numerically with those observed in experiments ([18],[17]). The present study used both finite element simulations and linear stability analysis to indicate that hexagonal cells are the preferred mode for the evolution of homogeneous systems at around the critical point for $Pr = 7$.

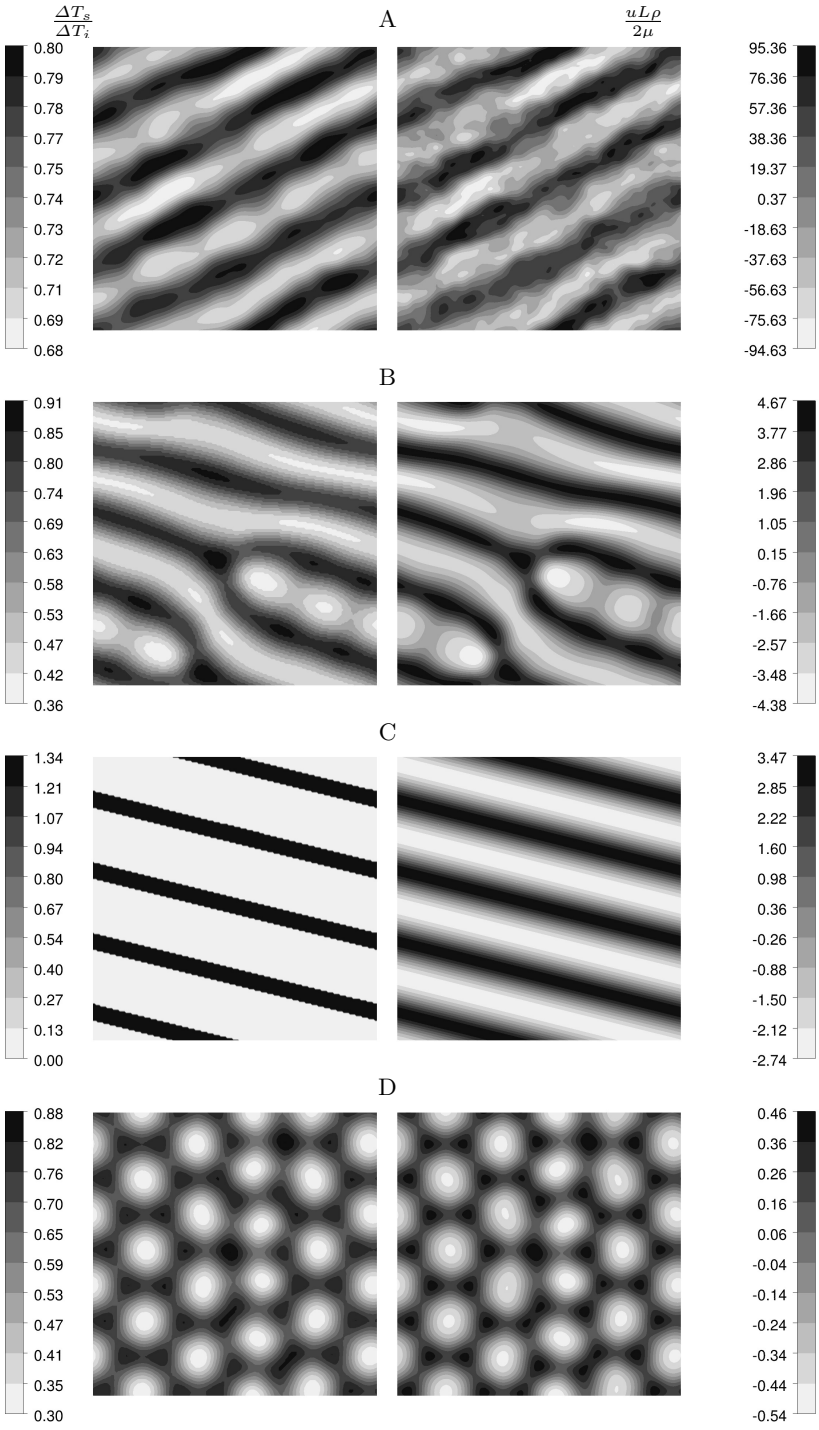

Fig. 5. Non-dimensional temperature (left) and vertical velocity (right) contours on the midplane in Figure 1, for different Pr at $\varepsilon = 2$. Here $\Delta T_s/\Delta T_i = |T - T_{\min}|/\left(Gr\mu^2\right)/\left(g\rho^2\beta\, L^3\right)$. A: $Pr = 0.005$; B: $Pr = 0.705$; C: $Pr = 0.883$; D: $Pr = 8.933$.

Beyond $\varepsilon = 6$ at $Pr = 7$, the finite element code predicts that the secondary structures deform resulting in different possibly rectangular states that are qualitatively comparable with the experimental studies of the Takeda group ([18],[17]). Between $\varepsilon = 1$ and $\varepsilon = 3$ the changes in orientation of the structures indicates that there is no preference in their orientation. Further non-linear analyses are being performed to explore the stability of the flow patterns observed at the transition to convective flow for a homogeneously heated layer with asymmetric boundary conditions.

Acknowledgements

The work presented here was funded by a Marie-Curie Intra-European Fellowship (Project No. 274367) for the European Commission and by the Royal Academy of Engineering Distinguished Visiting Fellowship Scheme. We wish to thank the Institute for Safety Research at the Helmholtz-Zentrum Dresden-Rossendorf for kindly allowing access to the computational cluster upon which the computational fluid dynamic calculations were performed.

Nomenclature

c_p	specific heat capacity at constant pressure, J kg^{-1} K^{-1}
Gr	Grashof number, $Gr = g\beta\rho^2 S_i L^5/2\mu^2 k$
Gr_c	critical Grashof number, Gr_c
$\boldsymbol{g}$	vector of the acceleration due to gravity, m s^{-2}
g	acceleration due to gravity, m s^{-2}
k	thermal conductivity, W m^{-1} K^{-1}
L	characteristic length, 0.007 m
Pr	Prandtl number, $Pr = c_p/\mu k$
p	pressure, kg m^{-1} s^{-2}
Ra	Rayleigh number $Ra = GrPr$
Ra_c	critical Rayleigh number $Ra_c = 1386$
S_i	volumetric heat source $S_i = 2k\Delta T_i/L^2$, kg m^{-1} s^{-3}
$\boldsymbol{S}$	momentum source terms, kg m^{-1} s^3
T	temperature, K
T_r	reference temperature, K
ΔT_i	initial temperature difference, $\Delta T_i = \left(Gr\mu^2\right) / \left(g\rho^2\beta\ L^3\right)$, K
ΔT_s	temperature difference of the solved flow, K
t	time, s
$\boldsymbol{u}$	velocity vector, m s^{-1}
u, v, w	velocity vector components, m s^{-1}
x, y, z	direction vector components, m

Greek symbols

α	wavenumber
β	expansion coefficient, 1/K
ε	reduced Grashof number = Gr/Gr_c

θ	non-dimensional temperature
μ	dynamic viscosity, kg m^{-1} s^{-1}
ϖ	non-dimensional pressure
ρ	density, kg m^{-3}
σ	eigenvalue
$\boldsymbol{\upsilon}$	non-dimensional velocity vector

References

1. ANSYS® CFX 12. *Theory Guide*, Canonsburg, USA, 2009, ANSYS Inc.
2. F. J. Asfia and V. K. Dhir. An experimental study of natural convection in a volumetrically heated spherical pool bounded on top with a rigid wall. *Nucl Eng Des*, 163:333-348, 1996.
3. R. C. Briant and A. M. Weinberg. Molten fluorides as power reactor fuels. *Nucl Sci Eng*, 2:797-803, 1957.
4. F. H. Busse. The stability of finite amplitude cellular convection and its relation to an extremum principle. *J Fluid Mech*, 30(4):625-649, 1967.
5. F. H. Busse. Fundamentals of thermal convection. In W. R. Peltier, editor, *Mantle Convection. Plate Tectonics and Global Dynamics (Fluid mechanics of astrophysics and geophysics vol 4)* pages 23-95, New York, 1989. Gordon and Breach.
6. G. M. Cartland Glover and S. C. Generalis. Pattern competition in homogeneously heated fluid layers. *Eng Appl Computat Fluid Mech*, 3(2):164-174, 2009.
7. R. M. Clever and F. H. Busse. Hexagonal convection cells under conditions of vertical symmetry. *Phys Rev E*, 53(3):2037-2040, 1996.
8. S. Generalis and M. Nagata. Transition in homogeneously heated inclined plane parallel shear flows. *J Heat Tran*, 125:795-803, 2003.
9. G. M. Gershuni, E. M. Zhukhovitsky and A. A. Yakimov. On stability of plane-parallel convective motion due to internal heat sources. *Int J Heat Mass Tran*, 17(7):717-726, 1974.
10. G. Houseman. The dependence of convection planform on mode of heating, Nature 332:346-349, 1988.
11. H. Ichikawa, K. Kurita, Y. Yamagishi and T. Yanagisawa. Cell pattern of thermal convection induced by internal heating. *Phys Fluids*, 18:038101, 2006.
12. M. Nagata and S. Generalis. Transition in convective flows heated internally. *J Heat Tran*, 124:635-642, 2002.
13. NIST. *NIST Chemistry WebBook*, Gaithersburg, USA, 2012, NIST.
14. P. H. Roberts. Convection in horizontal layers with internal heat generation. Theory. *J Fluid Mech*, 30(1):33-49, 1967.
15. J. Schmalzl, G. A. Houseman and U. Hansen. Mixing properties of three-dimensional (3-d) stationary convection. *Phys Fluids*, 7(5):1027-1033, 1995.
16. G. Schubert, G. A. Glatzmaier and B. Travis. Steady, three-dimensional, internally heated convection. *Phys Fluids*, 5(8):1928-1932, 1993.
17. J. Takahashi, Y. Tasaka, Y. Murai, Y. Takeda and T. Yanagisawa. Experimental study of cell pattern formation induced by internal heat sources in a horizontal fluid layer. *Int J Heat Mass Tran*, 53(7-8):1483-1490, 2010.
18. Y. Tasaka, Y. Kudoh, Y. Takeda and T. Yanagisawa. Experimental investigation of natural convection induced by internal heat generation. *J Phys Conf Ser*, 14:168-179, 2005.
19. Y. Tasaka and Y. Takeda. Effects of heat source distribution on natural convection induced by internal heating. *Int J Heat Mass Tran*, 48:1164-1174, 2005.

20. D. J. Tritton and M. N. Zarraga. Convection in horizontal layers with internal heat generation. *J Fluid Mech*, 30(1):21-31, 1967.
21. D. L. Turcotte, J. Schubert and G. Schubert. *Geodynamics*, second edition, pp. 280, Cambridge University Press, Cambridge, 2001.
22. M. Tveitereid and E. Palm. Convection due to internal heat sources. *J Fluid Mech*, 76:481-499, 1976.